Energy and Environmental Science

PAPER

Quantification of heterogeneous, irreversible lithium plating in extreme fast charging of Li-ion batteries: Electronic Supplementary Information

Partha P. Paul[a], Vivek Thampy[a], Chuntian Cao[a, b], Hans-Georg Steinrück[a, c], Tanvir R. Tanim[d], Alison R. Dunlop[e], Eric J. Dufek[d], Stephen E. Trask[e], Andrew N. Jansen[e], Michael F. Toney[a, b*], Johanna Nelson Weker[a*]

Section A: Details on the cells and cycling conditions

All cells were assembled at the CAMP facility at Argonne National Laboratory. The cells are made of single-layer graphite anode (3 mAh/cm^2, 14.9 cm^2 area, 71 µm thickness, 34.5 % porosity with a copper current collector), an NMC cathode (2.67 mAh/cm^2, 14.1 cm^2 area, 71 µm thickness, 34.5 % porosity with an aluminum current collector) and an EC:DMC (7:3) electrolyte with 1.2M $LiPF_6$ in a Celgard 2320 separator. The dimensions and components of the cell are shown in Fig. S1 while the assembly of the cell components is described in detail elsewhere[1]. Post assembly, the cells were tap charged and six formation cycles were put on the cells. The six formation cycles were followed by approx. two weeks of storage time, in the discharged condition. The capacity loss by each cell over the six formation cycles and the storage period is referred to as the '*formation capacity fade*', as tabulated in Table S1.

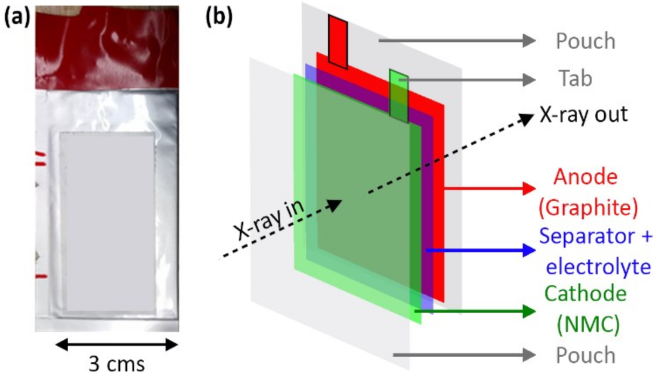

Fig. S1 Dimensions and components of the single layer pouch cells.

For XFC cycling, different C-rates and voltage-current protocols for charging were employed on different cells, as outlined in Table *S1*. The rationale behind choosing the C-rates and charging protocols has been discussed elsewhere[1]. All testing was performed at 30°C in an environmentally controlled chamber (TestEquity 1007C). A single thermocouple (Omega 5SC-TT-T-30-36, Type T) was placed near the positive electrode about 13 mm below the tab edge to measure the cell temperature during testing [2]. The thermocouple did not pick up any discernable temperature increase even at very high C-rates, e.g., 9C. The maximum temperature variation remained below 1°C. The placement of the thermocouple, heat generation (order of 1W) and quick heat rejection could have contributed to this observation. After cycle numbers 0 (i.e. first cycle after formation cycles), 25, 50, 75, 100, 125, 175, 225, 275, 325, 375 and 450, a slow cycle (C/20 rate) was done, to track of the capacity fade of the cell with cycling. The capacity of the cell lost during XFC cycling was calculated as the charge capacity during the 450th cycle, with respect to the charge capacity of the cell during the 0th cycle, henceforth referred to the '*XFC capacity fade*'. The total capacity lost by each cell is then given by adding up the contributions of formation cycles and XFC cycles to the capacity fade of the cell, per Equation S1. After 450 XFC cycles, we further discharged the cells at C/2 to 3V followed by a constant voltage hold at 3V until current reaches C/50 to ensure the cell reaches steady state at 3V and minimize any impacts of kinetic effects. Finally, the cells were shipped at 3.0V (discharged state) to Brookhaven National Laboratory (BNL) and Argonne National Laboratory (ANL), for XRD-based characterizations. The division of cells between ANL and BNL and the beam lines used are listed in Table S2. Note that the cells were stored at the fully discharged state for one to three months before XRD characterizations. Three of these cells are presented in an earlier work[1]. Cell **4C-a**, **9C-a** and **9C-b** presented here are labelled **cell 4**, **12** and **13** respectively in [1; 3].

$$Total\ capacity\ fade = formation\ capacity\ fade + (1 - formation\ capacity\ fade) \times XFC\ capacity\ fade \quad 1)$$

Cell	Formation capacity fade	Charge C-rate	XFC cycling protocol	XFC capacity fade	Total capacity fade
	(%)			(%)	(%)
4C-a	12.61	4C	CC-CV	7.09	18.80
4C-b	17.45	4C	Two-step CC	14.59	29.49
6C-a	16.80	6C	CC-CV	22.49	35.39
6C-b	15.92	6C	Two-step CC	19.69	32.71
6C-c	12.14	6C	Two-step CC	20.38	29.92
9C-a	13.07	9C	Five-step CC	27.97	37.38
9C-b	13.45	9C	Five-step CC	9.97	21.93

Table S1 Cells used for XRD-based characterization. All cells were cycled 450 times (after formation) at a discharge rate of C/2 and characterized in the fully discharged state, at a nominal SOC of 0%.

Cell	Charge C-rate	Beamline	Step Size
			(mm)
4C-a	4C	APS, 11-ID-B	1
4C-b	4C	APS, 11-ID-B	1
6C-a	6C	NSLS II, 28-ID-2	1
6C-b	6C	NSLS II, 28-ID-2	0.5
6C-c	6C	APS, 11-ID-B	0.5
9C-a	9C	NSLS II, 28-ID-2	1
9C-b	9C	NSLS II, 28-ID-2	0.5

Table S2 Experimental details on the XRD experiments for all the cells.

Section B: Calibration of experimental parameters for the XRD experiments

Details of the experimental set-up and calibration parameters for the XRD scans on the cells are provided in Tables S3 and S4.

Experimental Parameters	**Value**
Detector	Perkin Elmer XRD1621 digital imaging detector
Energy (Wavelength)	67 keV (0.1875 Å)
Calibration Parameters	
Calibrant	Ni
Sample to detector distance	1422.91 mm
Detector Tilt(s)	0.233°, 243.67 °
Pixels on detector	2048 x 2048

Table S3 Calibration parameters for **cells 6C-b**, **6C-c**, **9C-a, 9C-b** done at 28-ID-2 at NSLS-II at BNL[4]. Calibration was done using the GSAS-II software package. [5]

Experimental Parameters	**Value**
Detector	Perkin-Elmer XRD 1621 amorphous silicon detector
Energy (Wavelength)	58.6 keV (0.2113 Å)
Calibration Parameters	
Calibrant	CeO2
Sample to detector distance	1231.26 mm
Detector Tilt(s)	0.27°, 108.57 °
Pixels on detector	(206.672, 202.113)

Table S4 Calibration parameters for **cells 4C-a, 4C-b, 6C-a** done at 11-ID-B at APS at ANL. The calibration was done on the GSAS-II software package.

Section C: XRD patterns used for data analysis

The XRD peaks used for plotting Fig. 2, 3 and 4, as well as Table 1 are shown in Fig. S2. (a) shows a representative XRD pattern for a Q range from 0.5 $Å^{-1}$ to 3.6 $Å^{-1}$, which contains all the peaks used in the analyses. In particular, (a) shows the NMC $(0\ 0\ 3)$ peak (**Q** ~ 1.32 $Å^{-1}$) and graphite $(0\ 0\ 2)$ peaks (**Q** ~ 1.87 $Å^{-1}$), which are used in Table 1. (b, c) show smaller subsets of **Q** from (a). In particular, (b) shows the peak from staged graphite species (C_6Li, $C_{12}Li$) while (c) shows the peak for plated Li (we show the most intense Li peak across the entire cell for ease of visualization), with the red dotted line representing the background, which is described in detail in Paul et al. [1; 3] Peaks from staged graphite and Li are relatively lower in intensity, compared to the Cu, Al, NMC and pristine graphite peaks. However, we note that all the peaks of interest used in the calculations are well separated from each other. The main exception is LiC_6, where the $(0\ 0\ 1)$ and $(1\ 0\ 0)$ are adjacent to each other (**Q** ~ 1.68 and 1.70 $Å^{-1}$ respectively). However, since the $(0\ 0\ 1)$ is approx. 33 times the intensity of the $(0\ 0\ 1)$ peak, we consider the integrated intensity for LiC_6 coming from just the $(0\ 0\ 1)$ peak in Equation 1. For the NMC unit cell volume calculations outlined in Section F, all NMC peaks that overlap with other peaks (such as $(1\ 0\ \bar{4})$ and $(1\ 0\ \bar{2})$) are excluded from the analysis. An example of a fit for a representative NMC $(0\ 0\ 3)$ peak is shown in (d). All XRD patterns in Fig. S2 are from **Cell 9C-a**. The time required to capture an XRD pattern as in Fig. S2 (including the time for motion of the stage motors, exposure time, readout time from the detector, and writing of the data) is just below 4 seconds. This translates to the full cell scan, such as for **Cell 9C-a**, taking just under 3 hours with ~2500 data points.

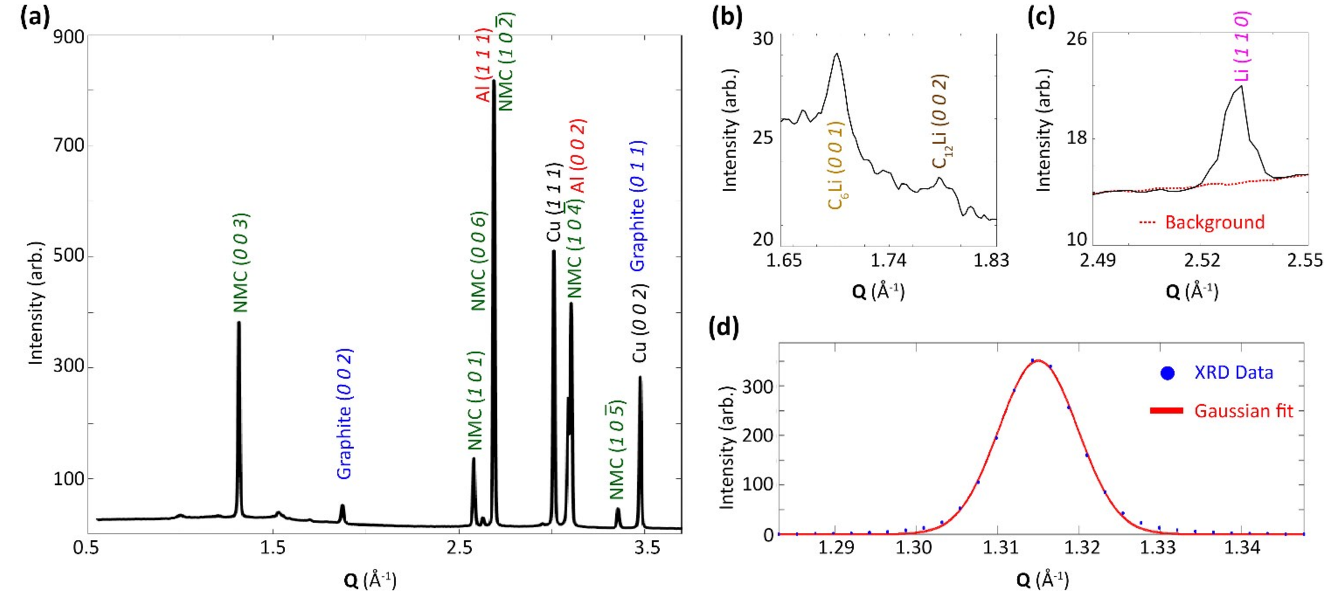

Fig. S2 Examples of XRD patterns used for the analysis in this work. (a) The full XRD pattern from ***Q*** = 0.5 Ǎ$^{-1}$ to 3.6 Å^{-1} with peaks from Cu, Al, NMC and graphite labelled. The relatively weaker peaks of (b) staged graphite and (c) plated Li, which are not easily visible in (a). The unlabelled small peak around ***Q*** = 1.0 Å^{-1} is a polymer peak, from the pouch material. A strong Li peak is shown in (c) for clearer illustration. (d) shows an example fit for determining the peak width and position for the NMC $(0\ 0\ 3)$ peak.

Section D: Spatial correlation between locally plated Li and cathode unit cell volume

For calculation of the NMC unit cell volume, peak positions from four NMC diffraction peaks are used. These are selected to show significant intensity and to be well separated from XRD peaks of other crystalline species in the cell. The peaks are $(0\ 0\ 3)$, $(1\ 0\ 1)$, $(0\ 0\ 6)$ and $(1\ 0\ 5)$. A Gaussian fit is used to obtain the peak positions. To obtain the NMC unit cell volume, lattice parameters *a* and *c* are calculated based on the d-spacing, $d_{h\,k\,l}$, which is related to the diffraction vector *Q* as $d_{h\,k\,l} = {}^{2\pi}/_{Q}$.

The four values of $d_{h\,k\,l}$ are used to obtain the two lattice parameters using least square fits. To account for the minor cell-to cell differences in the sample to detector distance, the peak positions for every NMC peak in each cell is calibrated against the known peak position of the copper current collector ($(1\ 1\ 1)$ peak is at *Q* = 3.0104 Å^{-1}). The peak widths are presented for the Gaussian fit of the NMC $(0\ 0\ 3)$ peak, since it can be directly correlated to lattice parameter '*c*', which changes with the lithium occupancy in the unit cell. Additionally, the $(0\ 0\ 3)$ peak is the brightest peak for NMC and is well separated from other peaks, making the fitting accurate. All the above data analysis steps are done on Matlab. Fig. S3 (a, b) shows the spatial correlations between the intensity of irreversibly plated lithium, and the SOC of the cathode, measured by the unit cell volume, for **Cells 9C-a, b**. The relationship between the plated lithium and anode species is shown in Fig. 4 in [1]. In both the cells in Fig. S2 as well as the cell in Fig. 2 (**Cell 6C-b**), the local regions of plated lithium on the anode side correspond to regions with a lower local SOC on the cathode side (represented by the NMC unit cell volume) and a higher variation in the cathode SOC (represented by the peak width of the NMC $(0\ 0\ 3)$ peak).

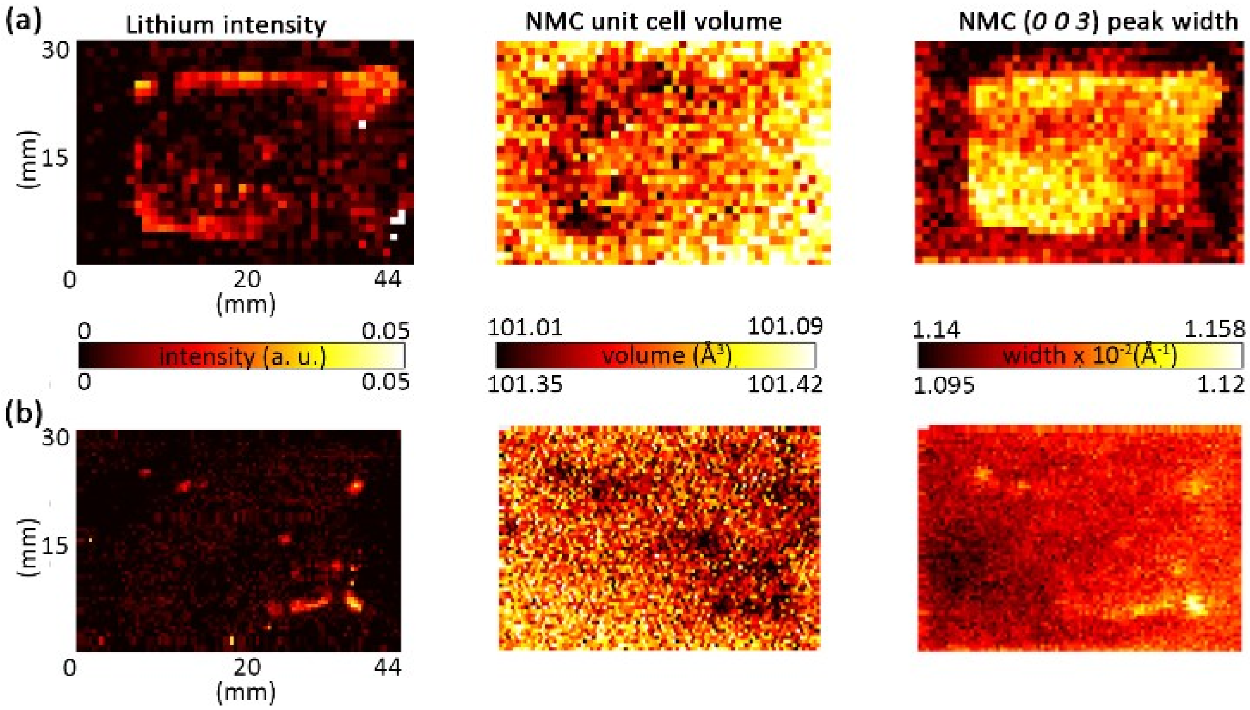

Fig. S3 Spatial correlations between local plated lithium on the anode (left) and the cathode SOC. The mean cathode SOC is shown by the NMC unit cell volume in the middle column while the variation in cathode SOC is shown in the right column, by the width of the NMC (*0 0 3*) peak. Row (a) shows the correlations for **cell 9C-a** while row (b) shows **cell 9C-b.**

Section E: Calculation of loss of active material and loss of lithium inventory from LiC$_6$ due to XFC cycling

The amount of LiC$_6$ and the associated LLI, as well as the LAM on the anode is a sum of components due to formation cycles and due to the XFC cycles. To calculate the loss of active anode material from XFC due to the trapped lithium as LiC$_6$ underneath the plated lithium (Fig. S4), three regions are selected arbitrarily in the cell such that two (Region 1, Region 3 – colored magenta) have little to no lithium plating and a third region has a significant amount of lithium plating (Region 2 – colored green). These regions are highlighted for **Cell 6C-b** in Fig. S3. Based on the ratio of intensity of LiC$_6$ to graphite, the amount of inactive anode material in Regions 1 and 3 is **~4%**, which is likely due to the formation cycles, while the amount of inactive graphite in Region 2 is **~25%**.

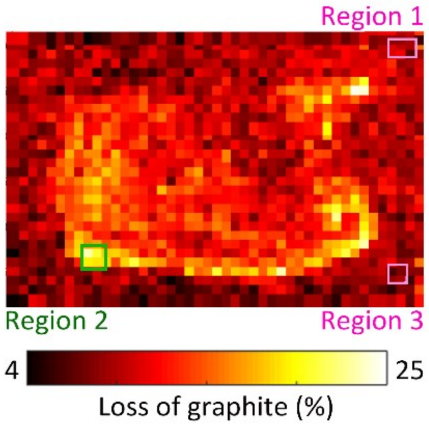

Fig. S4 Spatial map of the loss of active material on the anode side for **cell 6C-b**. The boxes highlight an area with a significant amount of lithium plating (Region 2, green box) and no lithium plating (Regions 1 and 3, colored magenta)**.**

To estimate the contribution of this XFC-generated LiC_6 to the LLI in the cell, this local analysis is extended to cover the entire cell. The average amount of LiC_6 from Regions 1 and 3 is multiplied by the area of the anode, to obtain the total amount of LiC_6 which is independent of Li plating. Subtracting this amount of LiC_6 from the total amount of LiC_6 in the cell furnishes the LiC_6 that is directly due to XFC cycling (lithium plating). Table S5 contains the LLI due to XFC cycling, as computed from the amount of LiC_6 in Regions 1 and 3. The mean of these two values is used to finally calculate the contribution of XFC cycling, and therefore Li plating to the LLI from LiC_6.

Cell	$\frac{I_{LiC_6}}{I_{NMc}} total$	**LLI (XFC C_6Li)**	**LLI (XFC - C_6Li)**	**Avg. LLI (XFC - C_6Li)**
	(x 10^{-3})	Region 1, (%)	Region 3, (%)	(%)
4C-a	6.4	-	-	-
4C-b	6.5	0.95	1.27	1.11
6C-a	8.7	1.99	1.61	1.80
6C-b	10.0	1.49	1.33	1.41
6C-c	9.5	1.57	0.84	1.21
9C-a	10.7	2.14	2.14	2.14
9C-b	10.6	0.10	0.68	0.39

Table S5 Separation of total LiC_6 into component due to XFC cycling (as trapped LiC_6 underneath the plated lithium).

Section F: Relationship between NMC unit cell volume and cathode SOC (Li occupancy)

Fig. 4 shows the linear relationship between the capacity retention in each cell with the average lithium occupancy in the NMC unit cell averaged over the entire cell. Table S6 shows the NMC unit cell volumes for each cell shown in Fig. 1, from which the average change in the NMC unit cell volume is calculated for each cell, with respect to the reference pristine cell. The change in unit cell volume is then converted to the average lithium occupancy per NMC unit cell, using the data shown in [6] from NMC532.

Cell	NMC unit cell volume	Δ (NMC unit cell volume)	Li occupancy	Capacity retention (formation + XFC)
	(Å^3)	(%)	(%)	(%)
4C-a	101.37	0.27	81	82.7
4C-b	101.30	0.38	73	71.6
6C-a	101.18	0.56	67	66.2
6C-b	101.23	0.49	69	72.0
6C-c	101.24	0.48	69	68.1
9C-a	101.15	0.63	65	63.5
9C-b	101.34	0.31	78	78.6
Pristine	101.54	0	102	100

Table S6 NMC unit cell volumes used for obtaining the average lithium occupancy per unit cell, using DeBiasi et al.[6]

References

[1] TANIM, T. et al. Heterogeneous Behavior of Lithium Plating during Fast Charging. **Cell Reports Physical Science**, p. 100114, 2020.

[2] TANIM, T. R. et al. Extreme Fast Charge Challenges for Lithium-Ion Battery: Variability and Positive Electrode Issues. **J. Electrochem Soc.,** v. 166, n. 10, 2019.

[3] PAUL, P. et al. Using in-situ X-ray Diffraction to Examine Behavior and Degradation of Lithium Ion Batteries from Extreme Fast Charging. **In Preparation**, 2021.

[4] SHI, X.; GHOSE, S.; DOORYHEE, E. Performance calculations of the X-ray powder diffraction beamline at NSLS-II. **Journal of Synchrotron Radiation,** v. 20, p. 234-242, 2013.

[5] TOBY, B. H.; VONDREELE, R. B. GSAS-II : the genesis of a modern open-source all purpose crystallography software package. **Journal of Applied Crystallography,** v. 46, p. 544-549, 2013.

[6] DEBIASI, L. et al. Between Scylla and Charybdis: Balancing Among Structural Stability and Energy Density of Layered NCM Cathode Materials for Advanced Lithium-Ion Batteries. **Journal of Physical Chemistry C,** v. 121, p. 26163−26171, 2017.